Journal of Computational Physics 229 (2010) 3828–3847

Contents lists available at ScienceDirect

Journal of Computational Physics

journal homepage: www.elsevier.com/locate/jcp

Modeling electrokinetic flows by the smoothed profile method

Xian Luo [a], Ali Beskok [b], George Em Karniadakis [a,*]

[a] Division of Applied Mathematics, Brown University, Providence, RI 02912, USA
[b] Aerospace Engineering Department, Old Dominion University, Norfolk, VA 23529, USA

ARTICLE INFO

Article history:
Received 23 September 2009
Received in revised form 11 December 2009
Accepted 25 January 2010
Available online 6 February 2010

Keywords:
SPM
Spectral elements
Poisson–Boltzmann equation
Electroosmosis and electrophoresis

ABSTRACT

We propose an efficient modeling method for electrokinetic flows based on the smoothed profile method (SPM) [1–4] and spectral element discretizations. The new method allows for arbitrary differences in the electrical conductivities between the charged surfaces and the surrounding electrolyte solution. The electrokinetic forces are included into the flow equations so that the Poisson–Boltzmann and electric charge continuity equations are cast into forms suitable for SPM. The method is validated by benchmark problems of electroosmotic flow in straight channels and electrophoresis of charged cylinders. We also present simulation results of electrophoresis of charged microtubules, and show that the simulated electrophoretic mobility and anisotropy agree with the experimental values.

1. Introduction

Electrokinetic flows have important applications in diverse fields such as biomedical, forensics, environmental and energy engineering [5,6]. The electrokinetic phenomenon occurs in heterogeneous fluids associated with an electric field. Due to various combinations of the driving force and moving phase, electrokinetic phenomena can be divided into several categories [7], among which *electroosmosis* and *electrophoresis* are two major effects. We first present a brief review of recent research progress on modeling electrokinetic flows.

Electroosmosis, or *electroosmotic flow* (EOF), is the electrically driven motion of a fluid relative to the stationary charged surfaces which bound it. One of the most useful applications of EOF is microfluidic pumping and flow control using electric fields [8,9], avoiding the use of mechanical pumps or valves with moving components. There are many experimental works which developed effective imaging techniques revealing interesting electroosmotically driven flows in various microscale geometries and with different coating materials [10–14]. There have also been many numerical simulations on EOF recently. Most of them are based on solving the Poisson–Boltzmann equation to include an electrokinetic force in the Navier–Stokes equation. A numerical algorithm based on the Debye–Hückel linearization was proposed in [15] to study electrokinetic effects in pressure-driven liquid flows. A finite-volume method was developed in [16] to simulate electroosmotic injection at the intersection of two channels. Beskok et al. have developed a spectral element algorithm for solution of mixed electroosmotic/pressure-driven flows in complex two-dimensional microgeometries [17–19]. Aluru et al. proposed meshless methods and compact models to study steady electroosmotic flows in microfluidic devices and also investigated the validity of the Poisson–Boltzmann equation in nanochannels using molecular dynamics simulations [20,21]. A lattice Boltzmann method was applied to study the electroosmosis in microchannels investigating chaotic advection and mixing enhancement by using heterogeneous surface potential distribution [22,23].

In contrast, *electrophoresis*, or *electrophoretic flow* (EPF) is the motion of charged particles relative to the stationary fluid. EPF can be thought of as the mirror image of EOF; both of them are due to the formation of electric double layer (EDL), which

* Corresponding author.
E-mail address: gk@dam.brown.edu (G.E. Karniadakis).

0021-9991/$ - see front matter © 2010 Elsevier Inc. All rights reserved.
doi:10.1016/j.jcp.2010.01.030

results from the interaction of the particle charges and the surrounding ionized solution. The electrophoretic motion is determined by a balance between the electric force due to the net particle charge under the EDL screening and the opposing hydrodynamic force. By taking advantage of the differences in the electrophoretic mobilities of different particles, separation and detection of macromolecules such as DNA, RNA, and microtubules is possible and useful in many fields like molecular biology and forensics [24,25]. Experimental techniques to measure the particle velocity in suspensions has been quite well-developed over recent decades, such as microelectrophoresis and electrophoretic light scattering [26]. Especially fluorescence microscopy can be used to image the electrophoretic motion of individual particles such as microtubules and virus particles, which are confined in microfabricated slit-like fluidic channels [27,28]. The measured electrophoretic mobility data are useful for estimating zeta-potential of dispersions based on established electrophoretic theories. The first complete analytical solution of the electrophoretic mobility for a sphere or a cylinder in an inertia-free flow was obtained by Henry [29], who investigated the so-called "retardation effects". Henry's formula takes as input an arbitrary electrical conductivity of the particles and the electrostatic potential distribution due to EDL. Further simplified formulations for the mobility have been derived by invoking the Debye–Hückel linearization under the assumption of small zeta-potentials [30–32]. More recently, O'Brien and White [33] developed perturbation methods and derived linearized equations to numerically compute the mobility, which allows for small deformation of EDL and thus includes the relaxation effect.

In contrast to the well-developed theories and analytical approximations, few full numerical simulations have been successful in resolving the electrophoretic flow. This is probably due to the difficulties of standard numerical methods for moving boundary problems, especially with charged complex boundaries. A finite element method, which uses a posteriori error estimation to adaptively refine the mesh, was proposed for solving the Poisson–Boltzmann equation around charged complex surfaces such as biomolecules [34,35]. This algorithm has the potential to be used in combination with an effective flow solver to simulate the electrophoresis of complex particles, but the computational cost associated with the remeshing is high.

More recently, a boundary-less method called the "Smoothed Profile" method (SPM), was proposed in [1,2] for solid–liquid two-phase flows. The key point of SPM is to update the velocity inside each particle through the integration of a "penalty" body force to ensure the rigidity of the particles. It imposes the no-slip boundary condition implicitly without any special treatment on the solid–fluid interfaces. Therefore, a fixed computational mesh can be used without conformation to the particle boundaries. We have previously improved this method for particulate flows by analyzing its modeling error and improving the discretization accuracy both temporally and spatially [4]. SPM was extended to account for the electrohydrodynamic coupling, by integrating the modified species conservation and Navier–Stokes equations [36,3,37,38]. In particular, it was applied to calculate the electrophoretic mobilities of charged spheres and showed great potential for modeling colloidal dispersions. However, due to the fully explicit time integration schemed used, the temporal stability and accuracy was not quite satisfactory. It has also been used in conjunction with uniform grids and simple particle shapes. Furthermore, the model used a uniform external electric field to calculate the electrokinetic force, which only works for particles with the same electrical conductivity as the surrounding electrolyte solution, and thus is not practical for general poorly-conducting materials.

The paper is organized as follows. In Section 2, we introduce the fundamental ideas of SPM. In Section 3 we propose an efficient modeling method for electrokinetic flows, allowing for spatially varying electrical conductivities. We include electrokinetic forces into the flow equations so that the Poisson–Boltzmann equation and electric charge continuity equations are cast into SPM forms. In Section 4, we verify the modeling method by benchmark problems of electroosmotic flow in straight channels and electrophoresis of charged cylinders. We present in the last section the simulation results of the electrophoresis of charged microtubules, and show that the simulated electrophoretic mobility and anisotropy agree with the experimental results. We conclude in Section 5.

2. Formulation

2.1. Smooth representation of particles

SPM represents each particle by a smoothed profile (or in other words an indicator/concentration function), which equals *unity* in the particle domain, *zero* in the fluid domain, and varies smoothly between one and zero in the solid–fluid interfacial domain. We use the following *general* form, which is effective for *any* particle shape:

$$\phi_i(\mathbf{x},t) = \frac{1}{2}\left[\tanh\left(\frac{-d_i(\mathbf{x},t)}{\xi_p}\right)+1\right], \tag{1}$$

where index i refers to the ith particle and $d_i(\mathbf{x},t)$ is the *signed* distance to the ith particle surface with positive value outside the particle and negative value inside the particle. Also, ξ_p is the local interface thickness, which can be either a constant or a variable as follows:

$$\xi_p = \xi \tag{2a}$$

$$\text{or} \quad = \xi \exp\left(-\frac{c|d|}{\xi}\right). \tag{2b}$$

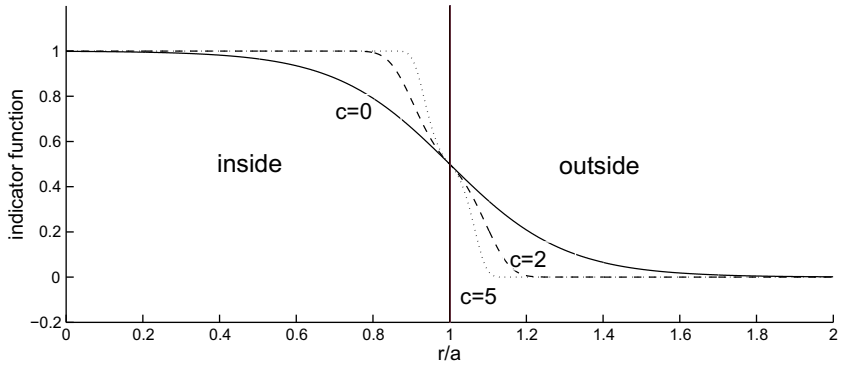

Fig. 1. Indicator functions for constant ($c = 0$) and variable ($c \neq 0$) thickness with $\xi/a = 0.3$.

Here, ξ is a constant representing the interface thickness parameter and typically $c = 2$; sharper profiles can be obtained for larger values of c as shown in Fig. 1. We see that for variable thickness (2b), $\xi_p = \xi$ at the particle surface ($d = 0$) and ξ_p decreases exponentially away from the surface.

A smoothly spreading *concentration field* is achieved by summing up the concentration functions of all the N_p non-overlapping particles:

$$\phi(\mathbf{x}, t) = \sum_{i=1}^{N_p} \phi_i(\mathbf{x}, t). \tag{3}$$

Based on this concentration field, the *particle velocity field*, $\mathbf{u}_p(\mathbf{x}, t)$, is constructed from the rigid motions of the N_p particles:

$$\phi(\mathbf{x}, t)\mathbf{u}_p(\mathbf{x}, t) = \sum_{i=1}^{N_p} \{\mathbf{V}_i(t) + \boldsymbol{\Omega}_i(t) \times [\mathbf{x} - \mathbf{R}_i(t)]\}\phi_i(\mathbf{x}, t), \tag{4}$$

where $\mathbf{R}_i$, $\mathbf{V}_i = \frac{d\mathbf{R}_i}{dt}$ and $\boldsymbol{\Omega}_i$ are spatial positions, translational velocity and angular velocity of the ith particle, respectively.

The *total velocity field* is then defined by a smooth combination of both the particle velocity field $\mathbf{u}_p$ and the fluid velocity field $\mathbf{u}_f$:

$$\mathbf{u}(\mathbf{x}, t) = \phi(\mathbf{x}, t)\mathbf{u}_p(\mathbf{x}, t) + (1 - \phi(\mathbf{x}, t))\mathbf{u}_f(\mathbf{x}, t). \tag{5}$$

We see that inside the particle domain ($\phi = 1$), we have $\mathbf{u} = \mathbf{u}_p$, i.e., the total velocity equals the particle velocity. SPM imposes indirectly the no-slip constraint and the no-penetration constraint on particle surfaces, which can be shown by taking the curl and divergence of the total velocity.

2.2. Modeling the electrical double layer (EDL) by PB equation

Most substrates (such as silica, glass, and certain polymeric materials) acquire charge when brought into contact with a polar medium, due to ionization or ion adsorption or ion dissolution. The resulting surface charge attracts the counter-ions (ions of opposite charge) and repels the co-ions (ions of the same charge) in the electrolyte, creating a layer of highly concentrated ions next to it which effectively screens the surface charge. This is known as the *electrical double layer* (EDL). The outer part of the screening layer that can move under the influence of tangential stress is referred to as the *diffuse layer*.

The characteristic thickness of the diffuse layer is the Debye length λ_d, which refers to the distance from the charged surface, where the electrokinetic potential energy equals the thermal energy. It is very common in the literature to use the reciprocal Debye length or the so-called Debye–Hückel parameter: $\kappa = \frac{1}{\lambda_d} = \sqrt{\frac{\sum_i e^2 z_i^2 n_{i,\infty}}{\epsilon\epsilon_0 k_B T}}$, where the subscript i indicates the ith ion species, e is the elementary charge, z_i is the ion algebraic valence, k_B is the Boltzmann constant, T is the absolute temperature, ϵ_o is the permittivity of vacuum, ϵ is the dielectric constant of the solvent and $n_{i,\infty}$ is the ionic concentration in the bulk solution.

The local electric potential ψ in the aqueous solution is related to the charge density through the Poisson equation of electrostatics:

$$\nabla^2\psi = -\frac{\rho_e}{\epsilon\epsilon_0} = -\frac{1}{\epsilon\epsilon_0}\sum_i ez_i n_i. \tag{6}$$

Here ρ_e is the net electric charge density, n_i is the local ionic concentration (number density) for the ith ion species, and the dielectric constant ϵ_0 is assumed to be uniform. In equilibrium state, the ion density in the diffuse layer obeys the Boltzmann

distribution [39,40]: $n_i = n_{i,\infty}\exp\left(-\frac{ez_i\psi}{kT}\right)$. This is consistent with the derivations based on statistical–mechanics theories [41]. It thus yields the famous Poisson–Boltzmann equation [42,7]:

$$\nabla^2\psi = -\frac{1}{\epsilon\epsilon_0}\sum_i ez_i n_{i,\infty}\exp\left(-\frac{ez_i\psi}{kT}\right), \tag{7}$$

which decouples the electric potential from ionic concentration and thus enables fast numerical simulations. The boundary conditions for Eq. (7) can be derived from either the zeta-potential ζ or the surface charge density σ_e. The former leads to a Dirichlet-type boundary condition ($\psi = \zeta$) and the latter to a Neumann-type $\left(\nabla\psi\cdot\mathbf{n} = -\frac{\sigma_e}{\epsilon\epsilon_0}\right)$ at the particle-solution interface Γ_p; $\mathbf{n}$ is the unit normal vector of the interface. Typically, for boundary conditions the zeta-potential is used instead of the surface potential, as it is the diffuse layer which obeys the Poisson–Boltzmann statistics and the Stern layer is usually very thin.

The Poisson–Boltzmann equation (7) can be rewritten in a dimensionless form for a binary electrolyte solution (i.e., $z_i = \pm 1$):

$$\nabla^2\psi_d = -\rho_{e,d} = \beta\sinh(\psi_d) \quad \text{in} \quad \Lambda_f \tag{8a}$$

$$\rho_e = \left(\frac{\epsilon\epsilon_0\zeta_e}{h^2}\right)\rho_{e,d}, \tag{8b}$$

where the subscript d refers to the non-dimensional quantities, e.g. the dimensionless charge density $\rho_{e,d} = -\beta\sinh(\psi_d)$. Also, $\beta = (\kappa h)^2$, h is the characteristic length used to normalize the length scale, and $\zeta_e = k_B T/ez$ (corresponding to 25.69 mV at 25 °C) is used to scale the electric potential as $\psi_d = \psi/\zeta_e$. We note that the equations are for the domain of the electrolyte solution Λ_f, and ρ_e refers to the charge density in the electrolyte solution. A spectral element algorithm has been developed to solve the PB Eq. (8) with *direct* boundary treatment at particle/solution interfaces [17–19]; it successfully resolves electroosmotic/pressure-driven flows in complex geometries.

For some electrokinetic problems, e.g., moving complex charged surfaces, the required remeshing for solving the Eq. (7) is challenging. To this end, we apply SPM to the Poisson–Boltzmann equation, aiming for an efficient modeling method for problems with moving EDLs induced by charged surfaces or bodies in an electrolyte solution. The direct implementation of the boundary conditions on the charged surfaces are removed, thus a simple computational mesh can be used. We modify the non-dimensionalized Poisson–Boltzmann equation (8) by specifying the charges on the immersed particles and extending to the entire domain Λ:

$$\nabla^2\psi_d = -\rho_{edl,d} = [(1-\phi)\beta\sinh(\psi_d) - \rho_{ep}] \quad \text{in} \quad \Lambda \tag{9a}$$

$$\rho_{edl} = \left(\frac{\epsilon\epsilon_0\zeta_e}{h^2}\right)\rho_{edl,d}, \tag{9b}$$

where ρ_{edl} is the total charge density in the double layer with its dimensionless form $\rho_{edl,d} = \rho_{ef} + \rho_{ep}$, and $\rho_{ef} = -(1-\phi)\beta\sinh(\psi_d)$, ρ_{ep} are the dimensionless charge density in the electrolyte solution and on the particles, respectively. Note that ϕ is the indicator function of Eq. (1).

We can adopt different forms of particle charge density ρ_{ep} due to different charge patterns:

$$\rho_{ep} = \gamma_v\phi \tag{10a}$$

$$= \gamma_s\nabla\phi \tag{10b}$$

$$= \gamma_s'\phi(1-\phi). \tag{10c}$$

Here γ_v and γ_s are the prescribed dimensionless volume or surface charge density, scaled by the total dimensionless volume $V_p = \int_\Lambda \phi d\mathbf{x}_d$ or total surface area $S_p = \int_\Lambda \nabla\phi d\mathbf{x}_d$ of the immersed particle, respectively. By recovering the dimensional equations, it is easy to show that $\gamma_s = \frac{h}{\epsilon\epsilon_0\zeta_e}e\delta_p$, where $e\delta_p$ is the surface charge density.

It is easy to show from Gauss's theorem that for symmetric shapes such as spheres and infinite circular cylinders, either the uniform surface charge or the uniform volume charge will result in exactly the same electric field and potential outside the particles.

As $\nabla\phi$ is not always analytically available for all particle shapes, and errors are introduced by the numerical differentiation, here we propose another way to introduce the surface charges as in Eq. (10c). We see that $\phi(1-\phi)$ has the expected peak at the surface, and γ_s' need to be scaled correspondingly to have the prescribed total charge.

For simplicity, only uniform volume charged or surface charged particles are considered, i.e., all γ in Eq. (10) are constant. However, we could also adopt a variable γ to simulate inhomogeneous charged particles.

2.3. Modeling the external electric field by the current continuity equation

Once an external electric field $\mathbf{E}_{ext}$ is applied, the charged surface and ions in the EDL will acquire some motion under the electric forces. Following the assumption made by Henry [29] that the applied field may be taken as simply superimposed on the electric field due to EDL, we consider separately when EDL effect is absent, how the applied uniform electric field is reconstructed near surfaces of insulators or with electrical conductivity different from the ionized solution. According to

Henry [29], the electrophoresis mobility would be much different, depending on whether or not the particles have the same electrical conductivity as the medium fluid.

The externally applied electric field $\mathbf{E}_{ext} = -\nabla\psi_{ext}$ and potential ψ_{ext} are governed by the current continuity or the charge conservation equation:

$$\nabla \cdot \mathbf{i} = -\nabla \cdot (\sigma \nabla \psi_{ext}) = -\frac{d\rho_{ext}}{dt}, \tag{11}$$

where $\mathbf{i}$ is the current density, σ is the electrical conductivity and ρ_{ext} is the charge density due to the conductivity difference. The relation used $\mathbf{i} = \sigma \mathbf{E}_{ext}$ is an expression of Ohm's law, with the assumptions of no charge convection and no ordinary diffusion [7], which is generally satisfied in the cases we are studying in this paper.

If we assume the charge distribution (due to the conductivity difference) is in quasi-equilibrium state, the last term in Eq. (11) vanishes, and we derive the following equation:

$$\nabla \cdot (\sigma \nabla \psi_{ext}) = 0, \tag{12}$$

where σ could either be the conductivity of the fluid medium σ_f or the one of the immersed particles or boundaries σ_p. That is, $\sigma = \sigma_f H(d) + \sigma_p(1 - H(d))$, where d is the distance to the interface and H is the Heaviside step function which is one in fluid medium and zero in particles. If both σ_f and σ_p are constants, (12) breaks into two Laplace equations:

$$\nabla^2 \psi_{ext,f} = 0 \quad \text{in} \quad \Omega_f \tag{13a}$$

$$\nabla^2 \psi_{ext,p} = 0 \quad \text{in} \quad \Omega_p \tag{13b}$$

where Ω_f, Ω_p are domains of fluid medium and particles, respectively. The boundary conditions for the applied potentials are:

$$\nabla \psi_{ext,f} = -\mathbf{E}_\infty \quad \text{at} \quad \infty \tag{14a}$$

$$\psi_{ext,f} = \psi_{ext,p}, \quad \text{at} \quad \Gamma_p \tag{14b}$$

$$\mathbf{s} \cdot (\nabla \psi_{ext,f}) = \mathbf{s} \cdot (\nabla \psi_{ext,p}) \quad \text{at} \quad \Gamma_p \tag{14c}$$

$$\mathbf{n} \cdot (\sigma_f \nabla \psi_{ext,f}) = \mathbf{n} \cdot (\sigma_p \nabla \psi_{ext,p}) \quad \text{at} \quad \Gamma_p \tag{14d}$$

where Γ_p refers to the interface with conductivity jumps, $\mathbf{E}_\infty$ is the external field strength in far field, and $\mathbf{s}$, $\mathbf{n}$ are the unit tangential and normal vectors of the surfaces Γ_p, respectively.

We note that for arbitrary non-zero σ_p, Eq. (13) need to be solved in both domains with coupled boundary conditions (14); this challenges the numerical solvers, as general direct methods only simulate the fluid domain. Also, the field $\mathbf{E}_{ext}$ is discontinuous with finite jumps across the interface Γ_p although the potential ψ_{ext} is continuous. This non-smooth nature of the exact solution causes great challenges to numerical discretizations. The spectral method with truncated expansions of polynomials suffers from the Gibbs phenomenon. Therefore, we propose a smooth approximation of the Eq. (12) as follows:

$$\nabla \cdot (\sigma \nabla \psi_{ext}) = \nabla \cdot ([\phi\sigma_p + (1-\phi)\sigma_f]\nabla \psi_{ext}) = 0 \quad \text{in} \quad \Omega, \tag{15}$$

where σ_p, σ_f are the electrical conductivity of the particles and surrounding fluid medium, respectively, and the equation is solved in the entire domain Ω. We use a smooth function ϕ to approximate the conductivity jumps across the interfaces between particles and surrounding solution as $\sigma = \phi\sigma_p + (1-\phi)\sigma_f$. Therefore, the boundary conditions on the particle surfaces are avoided and we impose only the far field condition, which normally would be $\nabla\psi_{ext} = \mathbf{E}_\infty$. This condition serves as a Neumann condition to be imposed on the boundaries of the computational domain. Alternatively, if our simulation domain includes the electrodes, we have boundary conditions from the known electrode potential: $\psi_{ext} = \zeta_{ext}$, which is a Dirichlet type boundary condition.

We apply the spectral element method to discretize Eq. (15) and to solve its weak variational form. An iterative (conjugate gradient) method is used to update the solution until the residual is reduced beyond a certain level (typically 10^{-12}). As the applied electric field and the resulting charge density have jump discontinuities in the exact solution, we use Galerkin projections to solve the following equations:

$$\mathbf{E}_{ext} = -\nabla\psi_{ext}, \tag{16a}$$

$$\rho_{ext} = -\epsilon\epsilon_0 \nabla^2 \psi_{ext}. \tag{16b}$$

A better approach would be to adopt a discontinuous Galerkin formulation, but this requires change in the expansion bases of our current spectral element solver.

2.4. Modeling electrohydrodynamic coupling by the Navier–Stokes equations

Providing the solutions for both the electric potential due to EDL and the externally applied electric field, we can couple the electrokinetic effects with the hydrodynamic motion by adding an electrokinetic force. Assuming the fluid medium to be incompressible and Newtonian with constant viscosity, the incompressible Navier–Stokes equations are used to solve for the total velocity $\mathbf{u}$ in the entire domain D:

$$\frac{\partial \mathbf{u}}{\partial t} + (\mathbf{u}\cdot\nabla)\mathbf{u} = -\frac{1}{\rho}\nabla p + \nu\nabla^2\mathbf{u} + \mathbf{g} + \mathbf{f}_s + \mathbf{f}_{\text{ek}} \quad \text{in} \quad \Omega, \tag{17a}$$

$$\nabla\cdot\mathbf{u} = 0 \quad \text{in} \quad \Omega. \tag{17b}$$

Here, $\mathbf{f}_s$ is the body force density term representing the interactions between the particles and the fluid. SPM assigns $\int_{\Delta t}\mathbf{f}_s dt = \phi(\mathbf{u}_p - u)$ to denote the momentum change (per unit mass at each time step) due to the presence of the rigid particles. Also, we have that $\mathbf{f}_s \sim \frac{1}{\Delta t}\phi(\mathbf{u}_p - u)$, suggesting that SPM is similar to penalty methods [43,44], which incorporate constraints into the governing equations. Here $1/\Delta t$ serves as a penalty parameter; thus the smaller Δt is, the tighter the control of the rigidity constraint is. This leads to an optimum time step size for pure hydrodynamic flow modeling, based on the balance of the Stokes layer thickness and interface thickness, i.e. $\delta = 2.76\sqrt{\nu(\Delta t)_o} = 2\xi$ as documented in [4].

The last term $\mathbf{f}_{\text{ek}}$ is the electrokinetic force density, which includes the force both on the electrolyte solution and on the charged particles. It can be written in the form of:

$$\mathbf{f}_{\text{ek}} = \rho_{edl}\mathbf{E}_{ext} + \rho_{ext}\mathbf{E}_{edl} \tag{18a}$$

$$\text{or} \quad = \rho_{edl}\mathbf{E}_{ext}, \tag{18b}$$

where the second expression (18a) is a possible simplification when the second term is zero or negligible, e.g. in the electroosmosis in straight channels with an external electric field parallel to the walls. We recall that ρ_{edl} is the charge density in EDL, which includes the particle charges (9b), $\mathbf{E}_{edl} = -\nabla\psi$ is the corresponding electric field due to EDL, and $\mathbf{E}_{ext}, \rho_{ext}$ are the external applied field and corresponding charge distribution, respectively. Note that here we do not explicitly include the forces $\rho_{edl}\mathbf{E}_{edl}$ and $\rho_{ext}\mathbf{E}_{ext}$, as their effects are already included in the Poisson–Boltzmann equation and the current density equation. More specifically, if we consider the static charges and corresponding electric field in an equilibrium EDL, the electric force $\rho_{edl}\mathbf{E}_{edl}$ on any ion is balanced by the force due to the concentration gradient and thus all the ions and fluid mass are stationary i.e., $u \equiv 0$. A similar argument can be made if we consider only the applied field around stationary interfaces.

For temporal discretizations of Eq. (17), we developed a stiffly-stable high-order *splitting* (velocity-correction) scheme [4], in order to enhance stability and increase temporal accuracy, as follows:

$$\begin{cases} \frac{\mathbf{u}^s - \sum_{q=0}^{J_e-1}\alpha_q\mathbf{u}^{n-q}}{\Delta t} = \sum_{q=0}^{J_e-1}\beta_q[-((\mathbf{u}\cdot\nabla)\mathbf{u})^{n-q} + \mathbf{g}^{n-q} + \mathbf{f}_{\text{ek}}^{n-q}] \quad \text{in} \quad D, \\ \frac{\mathbf{u}^{ss}-\mathbf{u}^s}{\Delta t} = -\nabla p^* \quad \text{in} D, \\ \left(\nabla^2 - \frac{\gamma_0}{\nu\Delta t}\right)\mathbf{u}^* = -\frac{\mathbf{u}^{ss}}{\nu\Delta t} \quad \text{in} D, \\ \frac{\gamma_0\mathbf{u}^{n+1}-\gamma_0\mathbf{u}^*}{\Delta t} = \frac{\gamma_0\phi^{n+1}(\mathbf{u}_p^{n+1}-\mathbf{u}^*)}{\Delta t} - \nabla p_p \quad \text{in} D \end{cases} \tag{19}$$

where $\alpha_q, \beta_q, \gamma_0$ are the coefficients derived for the stiffly-stable scheme of J_e^{th} order ($J_e = 1$, 2, or 3) (see [45]). Here $\mathbf{u}^s, \mathbf{u}^{ss}, \mathbf{u}^*$ are intermediate velocity fields; the pressure is split into two parts: $p^{n+1} = p^* + p_p$ to have the intermediate velocity divergence-free. Also, $\mathbf{u}^{n-q}$ and $\mathbf{g}^{n-q}$ are the velocity and body force fields at previous time steps. The particle translational and angular velocities are updated using an Adam–Bashforth scheme for Newton's equations.

For spatial discretization of the above equations, we apply the spectral/*hp* element method (see [45]). This hybrid method benefits from both finite element and spectral discretization. Hence, the use of *smoothed* profiles in SPM preserves the high-order numerical accuracy of the spectral/*hp* element method.

3. Numerical verification

In this section, we verify the modeling method with SPM boundary treatment for several benchmark problems of electrokinetic flows induced by charged particles in ionized solutions under an applied electric field. The numerical results of electric potential and charge density are compared with analytical solutions but also with numerical results based on *direct* boundary treatment.

3.1. Accuracy of SPM–PB solver

3.1.1. EDL near charged plates

The formation of EDL near a charged plate in contact with an ionized solution is of fundamental importance for electroosmotic flows in microchannels. We simulate the problem to verify the modeling methods with modified Poisson–Boltzmann equations (9) prescribing charge density on the particles.

We consider two charged parallel plates, which are separated by a distance of $2h$ in y-direction, while an infinite length is assumed for the other two dimensions. The geometry and corresponding computational mesh is shown in Fig. 2(a), with two "smoothed particles" representing the two walls located at $1.0 \leqslant |\eta| \leqslant 1.2$; all length scales are non–dimensionalized by h. We use 32 hexahedral elements with a finer grid near the plates, and the polynomial order is chosen from $P = 6$ to $P = 14$ to check the convergence.

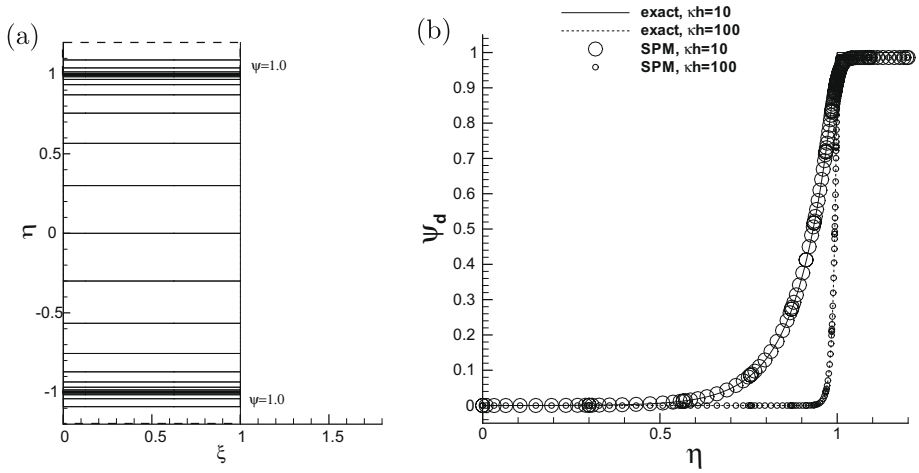

Fig. 2. *EDL in a channel with two charged walls*: Geometry of the channel (left) and profile of the dimensionless electric potential ψ_d versus interwall distance η compared to the exact solutions (right). Parameters used are $I = 0.741$, $\xi/\lambda_d = 0.1$ and $\kappa h = 10$ or 100. Only half of the domain is shown on the right plot due to symmetry.

We specify the surface charge density $e\sigma_e$ by using its dimensionless form $I = \frac{e\sigma_e}{\epsilon\epsilon_o} kT\lambda_d$, which is related to our dimensionless parameter in Eq. (10) through $I = \gamma_s/\kappa h$. In order to examine the numerical accuracy based on the charge specification, we determine the analytical zeta-potential from the Grahame equation [46]: $I = 2\sinh\left(\frac{\zeta_{exact}}{2}\right)$. Here, ζ_{exact} is the exact dimensionless zeta-potential scaled by kT/e, which we use as the "exact" solution. The assumption made in this equation is that the Debye length is very small compared to the particle dimensions $\kappa h = h/\lambda_d \gg 1$.

In order to examine the numerical results in a pointwise sense, we include for comparison the exact solution of the dimensionless potential given in [18]:

$$\psi_{exact,d} = 4\zeta_{exact}\tanh^{-1}[\tanh(1/4)\exp(-\kappa h(1-|\eta|))]. \tag{20}$$

Here it is assumed that the potential is zero at the channel center, i.e. $\psi_d(\eta = 0) = 0$. In order to have a fair comparison with the analytical results of ζ_{exact} and $\psi_{exact,d}$, we use small Debye length in our numerical simulations $\lambda_d/h \leqslant 0.1$. We plot the potential profiles across the channel in Fig. 2 (right), where the potential is scaled by ζ_{exact}. We see that SPM successfully resolves the potential variation in EDL for two sets of parameters used in our tests.

Fig. 3 presents the percentage errors in the zeta-potential $\frac{|\zeta-\zeta_{exact}|}{\zeta_{exact}} \times 100$. The error is mainly due to the modeling error of the smooth approximation used in (9), since the discretization error (spatial) is shown to be negligible by increasing the polynomial order beyond $P = 9$. The left plot shows that for a fixed Debye length, the error decreases with smaller interface thickness parameter ξ. It also shows that for a particular interface thickness used, the error goes up if we increase κh and

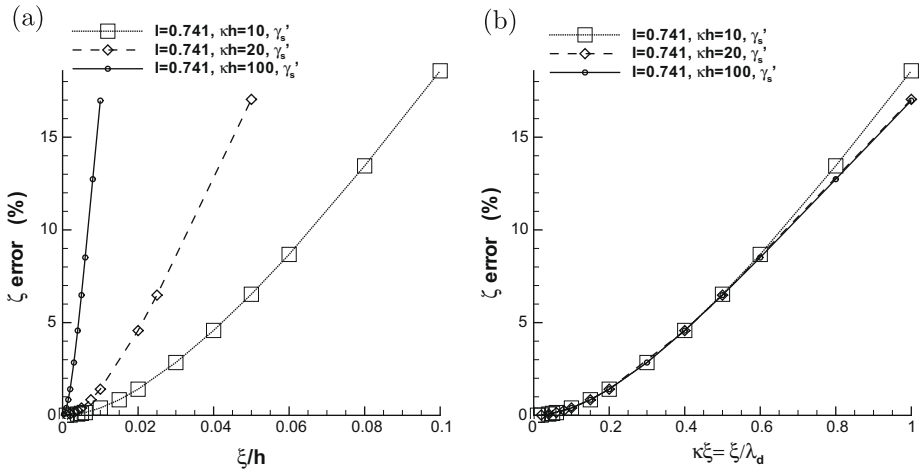

Fig. 3. *EDL in a channel with two charged walls*: Percentage error in zeta-potential with prescribed particle charge density (I) and Debye length ($\kappa h = h/\lambda_d$), showing the error dependence on the SPM interface thickness parameter (ξ/h) (a) and on the ratio of ξ/λ_d (b).

reduce the Debye length. In order to examine the error dependence on the ratio of interface thickness to Debye length $\kappa\xi$, we replot the same data in Fig. 3(b). The agreement in all the results for different Debye length indicates that the error is only dependent on the ratio $\kappa\xi$. This verifies that a better resolution of the double layer would be achieved if we use a smaller ratio $\kappa\xi$. In order to have a sufficiently good representation of the double layer with a characteristic thickness κ^{-1}, we need to use a relatively smaller SPM interface thickness. Recall that the effective interface thickness is scaled as $l_e = 2.07\xi$ (see [4]), so for adequate resolution, we propose that $2.07\xi < \lambda_d$, i.e. $\kappa\xi < 0.483$. This is verified by our numerical results, which show that the error is less than 6.5% if $\kappa\xi < 0.5$.

3.1.2. EDL around an infinitely long charged circular cylinder

Next, we consider a charged circular cylinder immersed in an electrolyte solution. The radius of the cylinder is $a = 11.0$ nm. We choose the scaling factor for length to be $h = 1$ nm and thus all the lengths in the rest of this section are dimensionless. The simulation domain is chosen to be $[-176, 176] \times [-176, 176] \times [0, 10]$, with a cylinder of radius $a = 11$ placed at the origin and its axis aligned with the z-axis. Note that a 3D simulation with a small spanwise dimension is used to study the 2D problem by a single layer of elements with periodicity imposed in the z-direction. For spatial discretization of SPM-PB Eq. (9), we use 1156 nonuniform hexahedral elements with polynomial order $P = 5$ or $P = 7$.

From the analytical approximation of Ohshima [47] for the surface charge density/surface potential relationship for a cylinder, we can obtain the exact zeta-potential ζ_{exact}, given the charge on the cylinder. The numerical errors of zeta-potentials are calculated and listed in Table 1 for a given dimensionless surface charge density $I = 1.47$ with $\kappa a = 1$. The results show that the error of the zeta-potential is less than 1% for all the interface thickness included, i.e., $\xi/a \leqslant 0.1$.

The Debye–Hückel approximate solution for a cylinder with low zeta-potential is used as a reference to compare with the numerical results:

$$\psi_{DH,cyl} = \zeta_{exact}\frac{K_0(\kappa r)}{K_0(\kappa a)}, \tag{21}$$

where K_0 is the zero order modified Bessel function of the second kind. Fig. 4 shows profiles of the dimensionless potential ψ_d along the radial distance to the cylinder center r. Here, we prescribe the total charge and Debye length as $I = 2.06, \kappa a = 11$ and investigate the effects of different particle charge patterns and smooth indicator functions. We see that the three sets of square symbols agree very well outside the cylinder and they verify the equivalence of the three different implementations of particle charge distribution in Eq. (10). Fig. 4 also shows significant improvement by decreasing the interface thickness parameter ξ, or by using a variable thickness ξ_p in Eq. (2b).

Percentage errors in zeta-potential $\left(\frac{|\zeta-\zeta_{exact}|}{\zeta_{exact}} \times 100\right)$ for various parameters are plotted in Fig. 5. Fig. 5(a) shows that for the case of $I = 1.47, \kappa a = 1$ and hence $\zeta_{exact} = 1$ (indicated by big symbols) the numerical error in ζ is less than 1% for all the values of the interface thickness such that $\xi/a \leqslant 0.1$.

The error increases if a higher charge density is imposed as $I = 22.64, \kappa a = 1$ and correspondingly $\zeta_{exact} = 6.08$, which is shown by the small hollow squares. However, we are able to reduce the error by using a variable interface thickness ξ_p as in Eq. (2b); the resulting error is less than 1.5% as long as $\xi/a \leqslant 0.1$, as shown by the small hollow circles. Similarly, we have greater numerical error when a smaller Debye length is presented $\kappa a = 11$, corresponding to the small filled symbols in Fig. 5(a). For such a small Debye length $\lambda_d/a = 0.09$, we need to use a sharper interface representation, either by reducing ξ or by using a variable ξ_p. We expect that in order to resolve the diffuse layer with a thickness scaled as λ_d, the effective smooth interface thickness needs to be bounded by the Debye length as $l_e = 2.07\xi < \lambda_d$. Our numerical results (filled squares) verify this statement by showing the error to be less than 7% if the above condition is satisfied; we note that this critical error is similar to the one obtained in the planar EDL simulations in Section 3.1.1. Furthermore, we are able to control the error to be within 2.5% if we use a variable interface thickness ξ_p with $\xi/a \leqslant 0.05$, as shown by filled circles in Fig. 5(a).

Fig. 5(b) demonstrates the error dependence on the reduced radius κa. It shows that for a fixed interface thickness ξ, the error grows with increasing κa and hence decreasing Debye length λ_d. The square symbols again confirm that the error is bounded by $\leqslant 7\%$, if we resolve the diffuse layer adequately by $l_e = 2.07\xi < \lambda_d$. Again, we improve the numerical accuracy by using a variable ξ_p, which is due to the resulting smaller effective interface thickness. It is indicated that no significant difference is caused by using different charge patterns, as either surface charge γ_s or volume charge γ_v.

Table 1
Electric potential of an infinitely long cylinder: dimensionless potential at the surface and the center of the cylinder with $I = 1.47, \kappa a = 1, \zeta_{exact} = 1$.

ξ/a	ζ	ψ_{center}	$error = \frac{\lvert\zeta-\zeta_{exact}\rvert}{\zeta_{exact}}$ (%)
0.01	0.999218	0.999890	0.0782
0.02	0.999675	0.999680	0.0325
0.03	0.999298	0.999299	0.0702
0.05	0.998151	0.998151	0.1849
0.1	0.993016	0.993016	0.6984

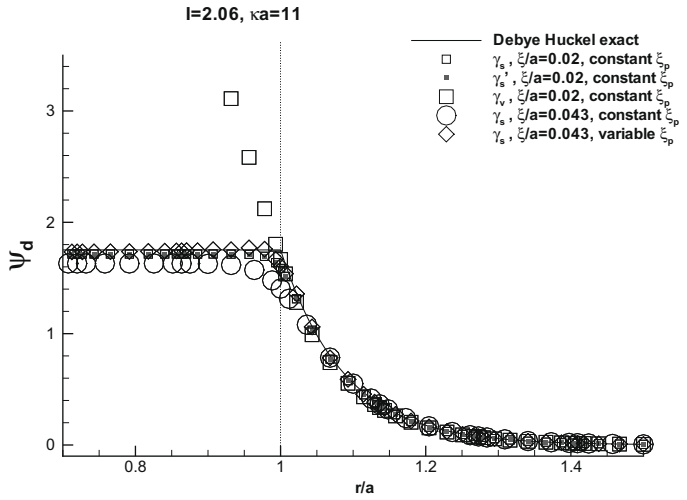

Fig. 4. *SPM simulations for EDL around an infinite cylinder*: Non-dimensional electric potential ψ_d versus radial distance r, compared to the Debye–Hückel approximation. The vertical dotted line indicates the cylinder surface.

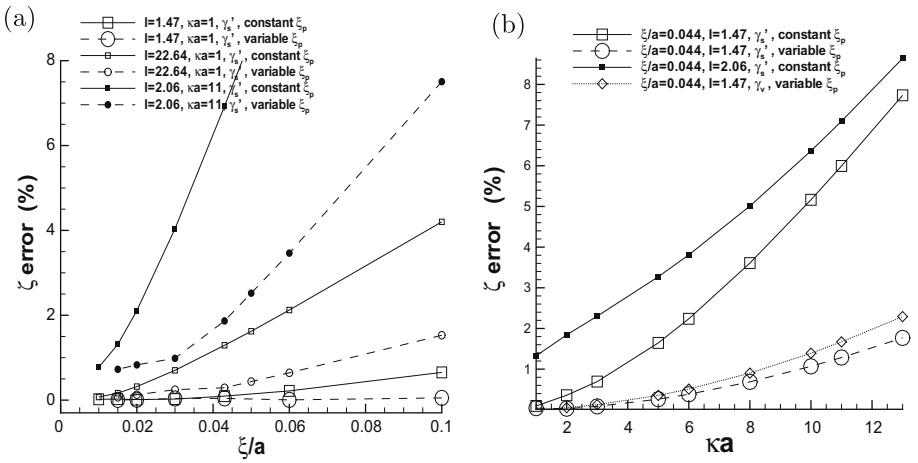

Fig. 5. *SPM simulations for EDL around an infinite cylinder*: Percentage error in dimensionless zeta-potential ζ_d for various dimensionless particle charge density (I) and charge distribution (γ), with dependence on (a): SPM interface thickness parameter (ξ/a) and (b): reduced radius (κa).

3.2. Accuracy of SPM current continuity solver

Next, we investigate the accuracy of the SPM solver of current continuity Eq. (15) by solving for the applied external electric field, which is distorted around poorly-conducting particles in an electrolyte solution with high electrical conductivity.

3.2.1. Applied field around a cylinder

We examine the accuracy of the SPM current continuity solver (15) for the applied electric field around an infinitely long circular cylinder. Same as the simulation setup for cylindrical EDL problems, a cylinder of radius $a = 11$ is aligned with z-axis, and a computational domain of $[-176, 176] \times [-176, 176] \times [0, 10]$ is used. The same spatial discretization is used, i.e. with 1156 nonuniform rectilinear (hexahedral) elements and polynomial order $P = 7$. Also, periodicity is imposed in the spanwise z-direction, but here we apply Neumann BCs for the other boundaries of the domain, i.e. $\frac{\partial \psi_{ext}}{n} = -\mathbf{E}_\infty \cdot \mathbf{n}$. The external electric field is uniform in the far field, i.e. $\mathbf{E}_\infty = (4000, 0, 0)$ V/m.

For comparison, we provide the exact solutions of the applied field and potential as follows:

$$\psi_{ext,out} = -\mathbf{E}_\infty \left(1 + \frac{\sigma_f - \sigma_p}{\sigma_f + \sigma_p} \cdot \frac{a^2}{(x^2 + y^2 + z^2)}\right) x, \tag{22a}$$

$$\psi_{ext,in} = -\mathbf{E}_\infty \left(1 + \frac{\sigma_f - \sigma_p}{\sigma_f + \sigma_p}\right) x. \tag{22b}$$

The exact electric field $\mathbf{E}_{ext,out}$ and $\mathbf{E}_{ext,in}$ is obtained correspondingly. These exact solutions can be applied at the domain boundaries as Dirichlet BCs; the resulting numerical solution is compared with the Neumann BC implementation to check the finite-domain effect.

We also include for comparison the SPM results using a limiting step function $\phi = H$ ($\xi = 0$) in Eq. (15), against the general SPM solution using a smooth ϕ ($\xi \neq 0$). So a curvilinear mesh conforming to the particle surface is employed for spectral element discretization, to avoid the Gibbs phenomenon due to the polynomial expansion in each spectral element. A total of 580 hexahedral elements with polynomial degree $P = 9$ are used for both cases: $\xi = 0$ and $\xi \neq 0$. The elemental mesh is shown in Fig. 6(b), with a comparison against the rectilinear mesh used for general smooth ϕ as in Fig. 6(a). We see that the results for the applied field by using these two different meshes are very similar.

Next we present near-field profiles of the applied electric potential in Fig. 7. The filled symbols in the figure show excellent agreement between the SPM results with $\xi = 0$ and the exact solution for all the conductivity ratios σ_p/σ_f included. However, note that due to the body-conforming mesh required, this model is not generally applicable, especially for complex boundaries or moving particles. The hollow circles corresponding to $\xi \leqslant 0$ show that the error grows with decreasing ratio σ_p/σ_f; while the outer field is resolved very accurately, worse accuracy inside the particle is observed. For the small ratio of $\sigma_p/\sigma_f = 0.001$, a small smooth interface thickness is required to resolve the interfacial field, e.g., $\xi/a = 0.01$ leads to errors under $L_\infty < 3\%$. Also, we note that the difference between using either rectilinear or curvilinear mesh is small, as shown by the small hollow symbols with identical $\sigma_p/\sigma_f = 0.1, \xi/a = 0.043$. This indicates that the results are mesh independent, and it suggests the use of simple rectilinear mesh regardless of the shape of the particles.

Fig. 8 presents numerical solutions of the applied electric field near the cylinder surface, with a small conductivity ratio $\sigma_p/\sigma_f = 0.001$. SPM results with various interface thickness ξ_p are compared against the exact solution and numerical solution with limiting $\xi = 0$. The agreement is very good for the outer field, but is worse inside the particle. By using a thin SPM interface of variable ξ_p with $\xi/a = 0.043$ and $c = 5$ in Eq. (2), the electric field at the center of the cylinder has a small error <2%, although some oscillations are present near the surface due to low resolution.

3.3. Accuracy of SPM electrohydrodynamic solver

In this section, we simulate the electrokinetic flows around simple particle shapes to investigate the accuracy of our SPM electrohydrodynamic solver (17).

3.3.1. Electroosmosis in a microchannel

We first consider the problem of EOF in a two-dimensional microchannel under the influence of an applied electric field, which is uniform and parallel to the channel walls. Since there is no distortion of the applied field due to the simple geometry, the electrokinetic force consists of only one term (Eq. (18a)) and thus the error from the current density solver is not included in the numerical results. The same geometry and computational mesh are used as for the planar EDL problem, see Fig. 2(a). Here we specify the non-dimensionalization factor $h = 0.5 \times 10^{-6}$ m for a channel of one micron wide. The other physical parameters are: the fluid density $\rho = 999.9$ kg/m^3, the dielectric constant $\epsilon\epsilon_o = 6.95 \times 10^{-10}$ C^2/J m, the dynamic viscosity $v = 0.889 \times 10^{-3}$ Pa s, the temperature $T = 25$ °C, and the external electric field $\mathbf{E}_\infty = (4000\,\mathrm{V/m}, 0, 0)$.

The analytical solution of the electroosmotic velocity is provided by Dutta [18] for zero pressure gradient and given the Stokes assumption:

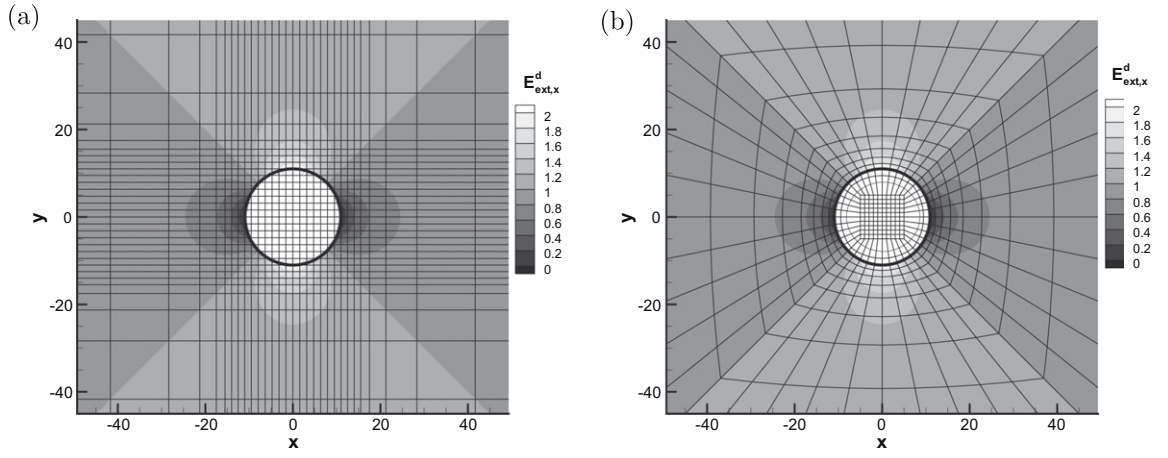

Fig. 6. *SPM simulations for applied field around an infinitely long cylinder*: Elemental mesh and contours of the external electric field $E^d_{ext,x} = E_{ext,x}/E_{\infty,x}$, with a conductivity ratios of $\sigma_p/\sigma_f = 0.001$ and interface thickness $\xi/a = 0.043$. The left plot refers to the rectilinear mesh and the right to the curvilinear mesh; the thick black curves indicate the cylinder surface.

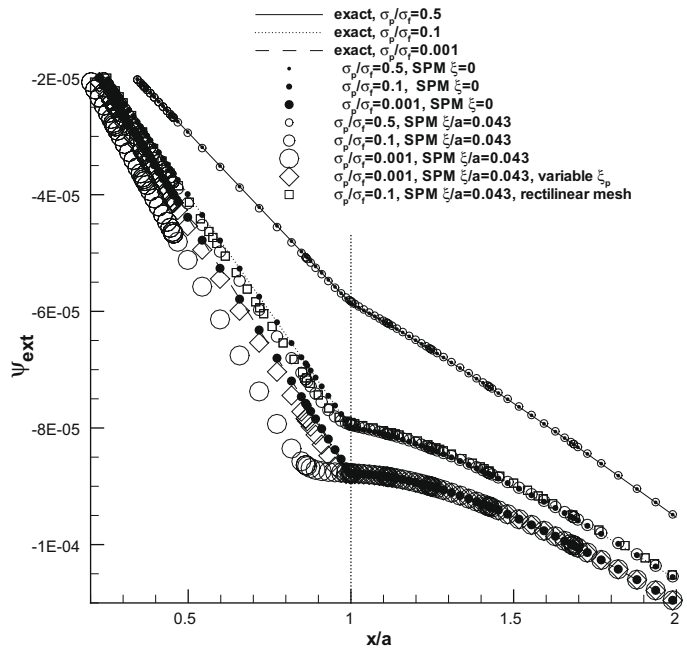

Fig. 7. *SPM simulations for applied field around an infinitely long cylinder*: External electric potential ψ_{ext} versus the primary axis x, with different conductivity ratios σ_p/σ_f. The dotted vertical line refers to the cylinder surface. A curvilinear mesh with Dirichlet BC is used if not indicated.

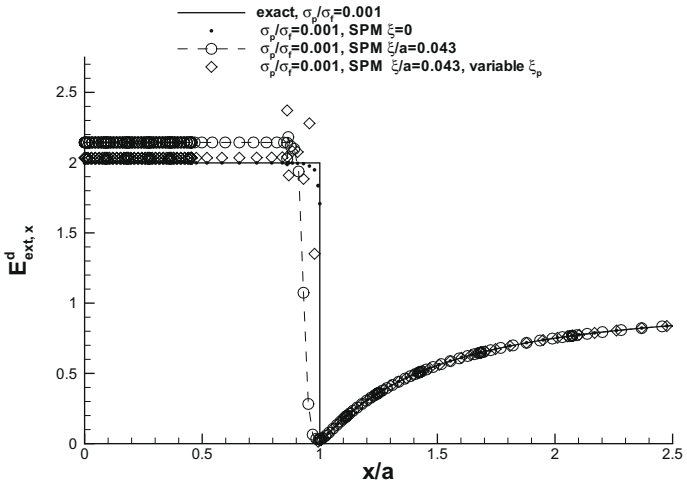

Fig. 8. *SPM simulations for applied field around an infinitely long cylinder*: The dimensionless external electric field $E^d_{ext,x} = E_{ext,x}/E_{\infty,x}$ along the primary axis x, with various SPM interface representations.

$$u^d_{exact}(\eta) = 1 - \frac{\psi_{exact,d}}{\zeta_{exact}}, \tag{23}$$

where $\zeta_{exact}, \psi_{exact,d}$ can be obtained from the Grahame equation [46] and Eq. (20) with the prescribed (dimensionless) charge density on the channel walls. Here, the velocity is scaled by the Helmholtz–Smoluchowski electroosmotic velocity $u_{\mathrm{HS}} = -\zeta_{exact}\frac{\epsilon\epsilon_0 E_\infty}{\mu}$, which is the velocity at the center of the channel assuming $\kappa h \gg 1$ and $\psi_{center} = 0$. We use this "exact" solution to verify our numerical results.

Fig. 9 shows typical velocity profiles across the channel. Note that we use the numerical solution of the electric potential and charge density in EDL with specified charge density $I = 0.741$ and thickness ratio $\kappa\xi = 0.1$ as in Fig. 2. We see that SPM successfully resolves the electroosmotic motion and shows that the velocity profile is more uniform for a smaller Debye length, i.e. larger κh. The figure also indicates that the numerical accuracy depends on the time step size used to iterate to a steady state.

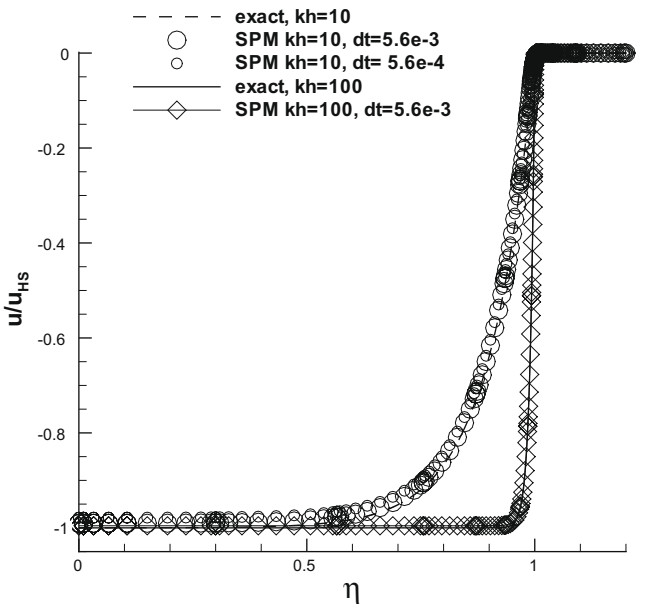

Fig. 9. *Electroosmosis in a microchannel*: Dimensionless streamwise velocity u/u_{HS} vesus interwall distance η compared to the exact solution (23), with different reciprocal Debye length $\kappa h = h/\lambda_d$ and computational time step dt.

In order to examine more closely this error dependence, we plot in Fig. 10 the percentage error of the center velocity $u(\eta = 0)$ compared to the Helmholtz–Smoluchowski results u_{HS}, i.e. $\frac{|u(\eta=0)-u_{\mathrm{HS}}|}{u_{\mathrm{HS}}} \times 100$. Again, we interpret the error as the modeling error of SPM, provided that both the temporal and spatial discretization errors are negligible. Note that this modeling error consists of three parts, i.e. the first one is due to the representation of rigid bodies by a penalty force in NS Eq. (17), which we have already quantified in [4]; the second one comes from the SPM–PB solver (9), which depends on $\kappa\xi$ as we showed in Section 3.1; the last part is attributed to the modeling error from the electrokinetic force constitution, which uses a smooth approximation of the EDL charges both on the particle and in the solution (9b).

Fig. 10 shows by the big symbols the error of velocity when we use the numerical solutions of EDL potential and charge from the SPM–PB solver (9). The error is very small (<1%) for the small Debye length $\lambda_d/h = 0.01$ for all time steps included, as shown by the big circles. Particularly, we note that the minimum error (around 0.43%) is consistant with the zeta-potential error from the SPM–PB solver, as shown by the dashed line, which is about 0.4% for both cases with different Debye lengths but the same thickness ratio. For a bigger Debye length $\lambda_d/h = 0.1$ as presented by the big squares, the error goes up, which may be partially due to the worse accuracy of the "exact" solutions for the zeta-potential and Helmholtz–Smoluchowski velocity, with the assumption of infinitesimally small Debye length. Furthermore, we note that in contrast to the non-monotonic error behavior of the pure hydrodynamic solver in [4], the modeling error of the electrokinetic solver is more like a monotonic function, which reaches a plateau beyond certain time step size.

In order to decouple the error of the SPM–NS solver from the SPM–PB solver, we show in Fig. 10 by the small symbols the velocity results when the exact solution of EDL potential (20) is used to calculate the charge density (9b) and thus the electrokinetic force. We see that the error dependence is non-monotonic, just as the error behavior from the hydrodynamic solver. However, the optimum time step is much bigger than the one from our previous analysis in [4]. An explanation can be put forth by a similar argument as in [4]. A smaller time step would have a tighter penalty control leading to better accuracy. However, a smaller time step also leads to a thinner Stokes diffusive layer $\delta = 2.76\sqrt{\nu dt}$ which is induced by the momentum impulse when imposing the rigidity constraint. If this thin Stokes layer is not resolved by the SPM interface $l_e = 2.07\xi$, it will result in a larger error. Similarly, this Stokes layer need to be thicker than the electric diffuse layer which has a characteristic length of λ_d, i.e. $\delta > \lambda_d$. So we conclude that the *optimum* time step comes from the balance of the Stokes diffusive thickness δ and the larger of the two: effective SPM interface thickness $l_e = 2.07\xi$ and Debye length λ_d. Our numerical results confirm this statement in Fig. 10(b), where dt_{λ_d} is the optimum time step expected from $\delta = \lambda_d$ (provided here $l_e < \lambda_d$). In fact, we can define an "effective" thickness of the electric diffuse layer λ_e by matching the numerical optimum time step to the relationship $\delta = \lambda_e$; our numerical data suggest that $\lambda_e = 1.25\lambda_d$ for this particular problem. We note that at such a distance away from the channel wall, the dimensionless potential drops to a value of $\psi_{exact}/\zeta_{exact} = 0.25$ according to Eq. (20). Hence, in general simulations with approximately planar surfaces we can use either of the two above conditions to obtain a good estimate of the optimum time step that minimizes modeling errors.

Furthermore, in Fig. 10 by comparing the results between the one using the numerical solutions of the SPM–PB solver and the one with the exact potential solution, we find that beyond certain time step size, the coupled electrokinetic solver leads to a "fortuitous" cancellation in the errors from SPM–PB and SPM–NS solutions, and this results in a plateau. Hence, for stea-

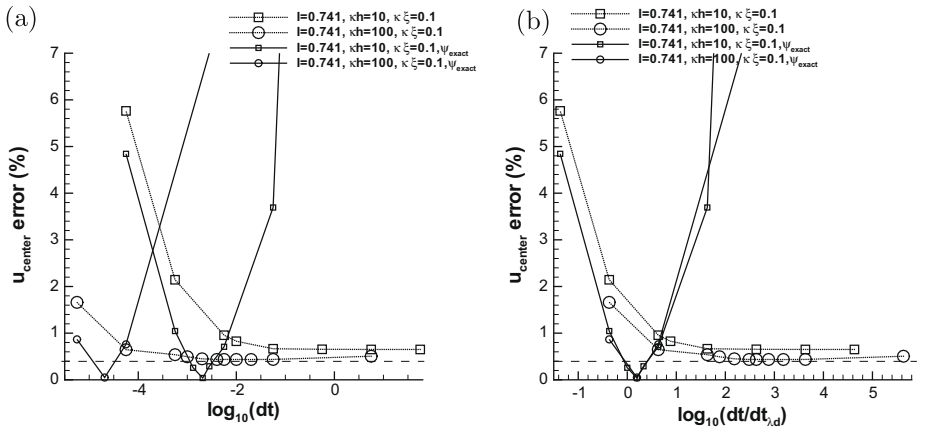

Fig. 10. *Electroosmosis in a microchannel*: Percentage error in centerline velocity versus time step size dt (a) and versus time step ratio dt/dt_{λ_d} (b), with specified particle charge density (I), reciprocal Debye length ($\kappa h = h/\lambda_d$ and thickness ratio $\kappa\xi$). Dashed line indicates the error in the zeta-potential from the SPM–PB solver.

dy states solutions obtained through our time-marching schemes very large time steps can be used for greater efficiency and better accuracy. For time-dependent simulations, however, the SPM-induced error has to be balanced with the temporal error for time-integration and this will give the optimum time step.

3.3.2. Electrophoretic mobility of a charged infinite cylinder in a transverse or a parallel electric field

Provided with the numerical solutions of the electric potential and field for both the EDL and the applied electric field in the presence of a particle, we can now verify the SPM electrohydrodynamic solver (17) by studying electrophoretic mobility. First, we study the problem of the electrophoretic flow around a charged infinite cylinder and in the next section we validate the new method against recent experiments on the electrophoretic mobility and anisotropy of microtubules.

We use the same computational configuration as in the EDL and the applied field simulations for a cylinder with $a = 11$. The domain $[-176, 176] \times [-176, 176] \times [0, 10]$ is discretized using 1156 nonuniform hexahedral elements and polynomial order $P = 7$. Also, periodicity is imposed in the spanwise z-direction.

We present comparisons with Henry's exact solution [29] for the electrophoretic velocity $(V_{p,Henry})$ of a cylinder in a transverse field, which was derived from the Stokes equation with Oseen's correction. The analytical expressions take as input an arbitrary conductivity ratio σ_p/σ_f and the electric potential solution due to EDL. Here we obtain the "exact" zeta-potential ζ_{exact} from the potential-charge relationship expression in [47], and use the Debye–Hückel approximation (21) for the "exact" potential field. It is assumed that the zeta-potential is small and thus linearization of the Poisson–Boltzmann equation is possible. The "exact" solution for the mobility with a parallel orientation is given by Smoluchowksi's formula: $V_{p\|} = u_{HS} = E_\infty \epsilon\epsilon_0 \zeta\eta$, where small Debye length is assumed $\kappa a \gg 1$. These analytical results are also used as the Dirichlet BC on the boundaries of the computational domain to alleviate the finite-domain effect.

We prescribe the dimensionless charge on the cylinder $(I = 2.06)$ with a reduced radius $\kappa a = 11$ and the undistorted external electric field $\mathbf{E}_\infty = (4000\,\mathrm{V/m}, 0, 0)$. For the small ratio of $\sigma_p/\sigma_f = 0.001$, Henry's solution indicates that $V_{p\perp} = 1.028\mathrm{e}-4$ for a cylinder perpendicularly oriented to the applied field and $V_{p\|} = 1.250\mathrm{e}-4$ for the parallel orientation; hence the anisotropy is $V_{p\perp}/V_{p\|} = 0.822$. However, if $\sigma_p/\sigma_f = 1$ and thus the external field is uniform, the transverse mobility and hence the anisotropy drops significantly, i.e. $V_{p\perp} = 6.249\mathrm{e}-5$ and $V_{p\perp}/V_{p\|} = 0.5$. Note that this anisotropy is exactly the same as that of an infinite cylinder in pure hydrodynamic flow.

Fig. 11 presents profiles of the streamwise velocity scaled by the Smoluchowksi velocity u_{HS} for a cylinder with a perpendicular orientation. All SPM results are using an indicator function of variable ξ_p with $\xi/a = 0.43, c = 2$ in Eq. (2b). The figure shows that SPM successfully resolves the electrophoretic flow features; it verifies that the mobility decreases with increasing conductivity ratio σ_p/σ_f.

Furthermore, Fig. 11 shows that the volume charge implementation γ_v results in an overshoot of the particle velocity, while the surface charge pattern γ_s' always leads to an undershoot. Since these two charge patterns have been verified to equivalently resolve the cylindrical EDL potential, the difference in the mobility comes from the inadequate resolution of the applied field near the interfaces, which results in an underestimation of the driving electric force for the surface charge.

We also include for comparison in Fig. 11 the numerical results for a pure hydrodynamic motion of a cylinder in a periodic box. The external non-electric force applied on the cylinder is set to be the same value as the electric force based on the total charge on the cylinder, i.e. $F_x = Q_p E_\infty = 1.015 \times 10^{-13}$ N. A negative uniform pressure gradient is applied on the fluid to ensure the zero net flux out of the domain. The velocity shown is scaled by the particle velocity $V_p = 1.53 \times 10^{-3}$, which is an order of magnitude larger than the typical electrophoretic velocity scale u_{HS}. The figure also shows that the electrophoretic motion has a much shorter disturbance length in the surrounding fluid, when compared to the pure hydrodynamic motion.

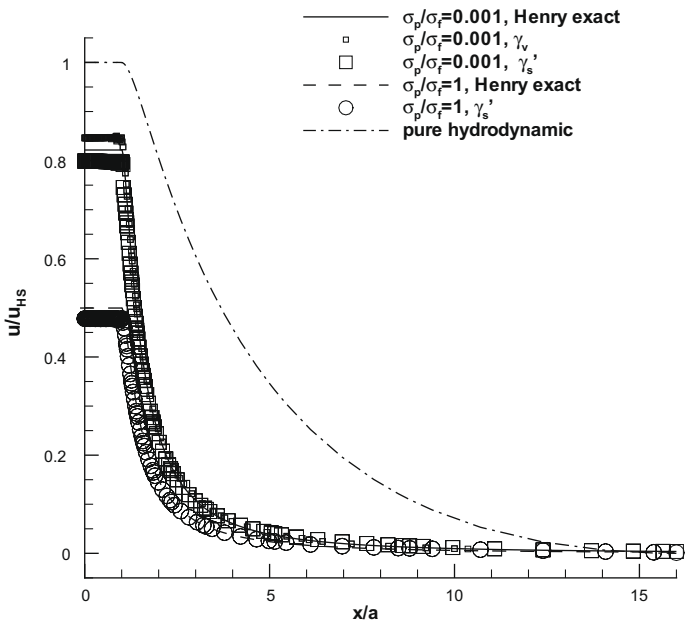

Fig. 11. *Electrophoresis of an infinite cylinder in a transverse electric field*: Dimensionless streamwise velocity along streamwise distance, compared to Henry's solution [29], with two different conductivity ratios σ_p/σ_f.

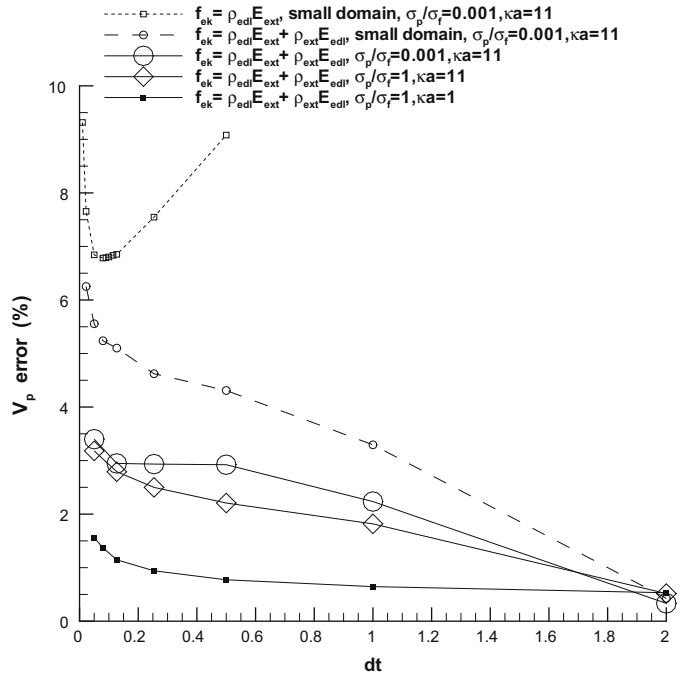

Fig. 12. *Electrophoresis of an infinite cylinder in a transverse electric field*: Percentage error in electrophoretic velocity versus time step, with a variable ξ_p and $\xi/a = 0.43$.

This is due to the opposite electric force on the surrounding fluid via the counter-ions, which is termed as the *retardation effect*.

In Fig. 12, the percentage error of the electrophoretic velocity $\left(\frac{|V_p - V_{p,Henry}|}{V_{p,Henry}} \times 100\right)$ is plotted versus the time step size used in the NS solver (17). As comparisions are made against Henry's solution for an infinite domain, we check the finite-domain effect by using an alternative mesh for a smaller domain, i.e. $[-114, 114] \times [-114, 114] \times [0, 10]$ with 1024 elements and

7th polynomial order. The figure indicates that increasing the size of the simulation domain leads to a smaller error, as shown by the circle symbols. It is also verified by the first two sets of small symbols that including both force components (Eq. (18)) leads to better accuracy.

Furthermore, comparison between the big symbols in Fig. 12 shows that by increasing the conductivity ratio to $\sigma_p/\sigma_f = 1$ (hence $\mathbf{E} = \mathbf{E}_{inf}$) and thus excluding the error from the current density solver, the error is reduced for most values of time steps, but it is still of a comparable scale. This suggests that the error comes mainly from the PB solver and the NS solver; we recall that the error in the zeta-potential is around 2% for the parameters used. Meanwhile, for a larger Debye length $\kappa a = 1$, the error in the electrophoretic velocity is below 2% for all the time steps involved, as shown by the filled squares. This is due to the better accuracy in the PB solution, since the error in the zeta-potential is as small as 0.3%. We also note that the error tends to form a plateau when the time step size goes beyond certain value, which is very similar to the error behavior in the electroosmotic flow problem. This again verifies that the coupling of the PB solution with the NS solution leads to a cancellation in the modeling error and thus tends to favor larger time steps.

4. Simulations: electrophoretic flows of microtubules

Microtubules have very complex structure. According to the results by an axial projection of the electron-density map [27,48], a single microtubule can be modeled as 13 protofilaments around a thin cylindrical shell, with an inner radius of $a_i = 8.4$ nm and an outer radius of $a_o = 9.5$ nm. Each protofilament is a half-ellipsoid with radius $a_a = 2.3$ nm and $a_b = 3.0$ nm. Due to this complexity in geometry, numerical simulations of the electrokinetic flow around microtubules with standard computational methods have not been reported before. Our SPM electrohydrodynamic solver is a good candidate for such a problem as it removes the difficulty on applying the boundary conditions for complex shapes.

We simulate the electrophoretic flow of an individual microtubule and aim to assess agreement with the experimental results in [27]. In order to examine how the surface roughness of microtubules affects the EDL, the applied field and thus the electrophoretic motion, we include for comparison the simulation results for a circular cylinder with a similar "effective" radius.

4.1. EDL of microtubules

According to [27], the Debye length is around $\lambda_d = 0.7$ nm and the surface charge density is about $e\delta_p = -36.7\times 10^{-3}$ C/m^2, corresponding to the dimensionless charge density $I = 1.39$. Thus, we set the corresponding charge density coefficient in Eq. (10) to be $\gamma_s = 1.992$, and γ_v, γ_s' are calculated correspondingly with fixed total charge. Note that although it is normally assumed that the microtubules are uniformly surface charged, the real charge distribution is uncertain. Therefore, we will use and examine both uniform surface charge and uniform volume charge patterns in our SPM–PB solver of Eq. (9).

The simulation domain is $[-176, 176] \times [-176, 176] \times [0, 10]$, with periodicity imposed in all directions. Note that the scaling factor for length is $h = 1$ nm and thus all the length scales in the section are dimensionless. We use 1156 nonuniform hexahedral elements with polynomial order $P = 7$ for spatial discretization with spectral element method. This mesh is used to simulate the EDL problem for a microtubule or a cylinder which is aligned with the z-axis. Different shapes are represented by different smooth indicator functions with analytical expressions of the distance to the surface. The interface thickness parameter is set to $\xi/a = 0.02$ for a good representation of the shapes by SPM. For comparisons with a microtubule, the cylinder adopts the same inner radius $a_i = 8.4$ and an outer radius of $a = 11.0$, which is chosen to match the average outer radius of the microtubule $a = a_o + a_b/2$.

To study the effect of hollowness in EDL potential variation, we begin with solid cylinders and "solid" microtubules and compare with the hollow structures. In Figs. 13 and 14 we plot the dimensionless electric potential contours in EDL around a microtubule with comparisons to a cylinder. We also present the value of the potential for typical spatial points. Here, $\psi_{surface}$ refers to surface points, ψ_{center} to the center, $\psi_{surface\_out}$ to the outer surface of cylinder (11,0,0), $\psi_{surface\_out,f}$ to the furthest outer surface point on microtubule (12.5,0,0), $\psi_{surface\_out,n}$ to the nearest outer surface point on microtubule (−9.5,0,0), and $\psi_{surface\_in}$ to the inner surface (8.4,0,0). Figs. 13 and 14 show that with surface charges, in contrast to the uniformity of the potential present in a cylindrical particle, the potential on the surface and inside a microtubule has big variations. This is due to the irregularity and asymmetry of the microtubule geometry. Although the surface charge density of a microtubule is assumed to be a constant, the charge on the surface near the protofilaments joints is higher than the rest of the surface; the relative difference in the potential between two typical surface points is as high as $\frac{\psi_{surface,out,n}-\psi_{surface,out,f}}{\psi_{surface,out,f}} = 54\%$. It is indicated in Fig. 14 that the hollowness does not influence much the potential distribution outside the cylinder or the microtubule, with a difference less than 10% in the surface potential when compared to the solid structures.

4.2. Applied electric field around microtubules

We apply the SPM current continuity solver (15) to solve for the applied external electric field around poorly-conducting microtubules in an electrolyte solution. Comparisons are made against the numerical results for an infinitely long hollow

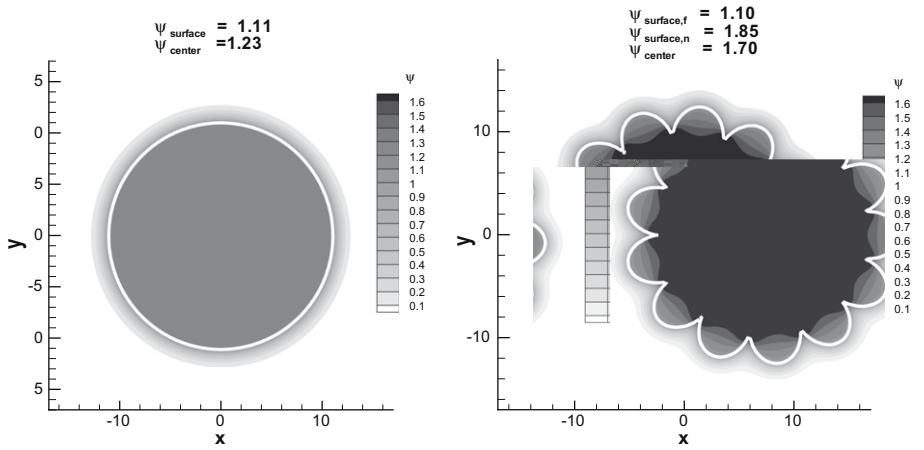

Fig. 13. *SPM simulations for EDL around a surface charged solid cylinder and a "solid" microtubule*: Contours of dimensionless electric potential due to electrical double layer, with identical surface charge density. The white curves indicate the particles' surfaces.

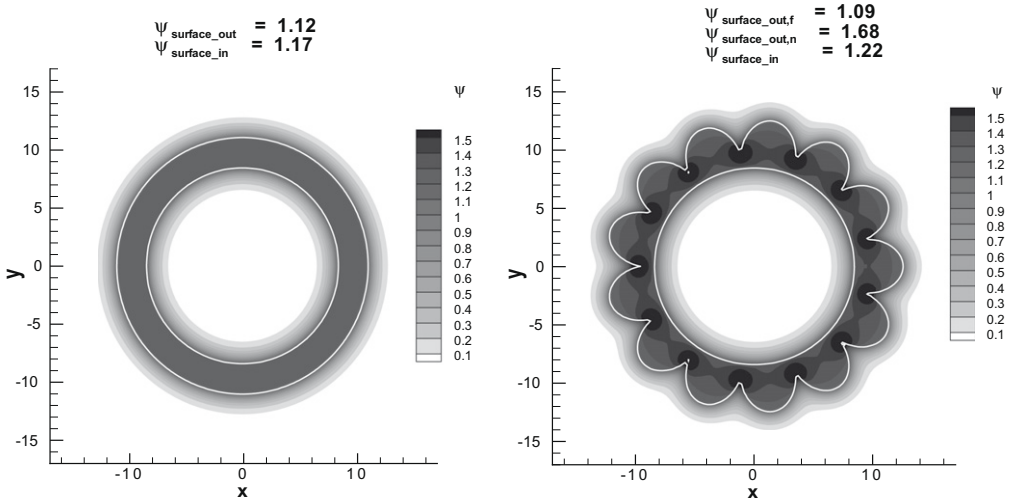

Fig. 14. *SPM simulations for EDL around for a surface charged hollow cylinder and a hollow microtubule*: Contours of dimensionless electric potential due to electrical double layer, with the same surface charge density as above.

circular cylinder with the same conductivity and effective radius. The same simulation domain and spatial discretization are used as for the EDL problem around a microtubule.

Fig. 15 shows that the electric field inside a hollow cylinder is much stronger than that inside a solid structure, which is $E^d_{ext,x} = E_{ext,x}/E_\infty = 2$ by the analytical solution (22b). A microtubule has a similar magnitude in the electric field as a hollow cylinder, but the field is distorted to a much greater extent due to the undulated surface geometry, as shown in Fig. 15(b). In particular, we note that the resulting field for a microtubule loses its symmetry in x-direction as expected from the asymmetric geometry; this suggests that the problem is orientation dependent.

4.3. Electrophoretic flows of microtubules

We apply the electrohydrodynamic solver (17) to study the electrophoretic motion of cylinders and microtubules, which are oriented either parallel or perpendicular to the external applied field. Typical numerical results of the electrophoretic velocity and anisotropy for various particles are listed in Table 2. Comparisons are made against the exact solution for an infinite solid cylinder by Henry [29]. The same reference surface charge density $I = 1.39$ is used for all the particles listed, so the hollow particles have more total charge due to the extra charge on the inner surface. In all the simulations, we use volume charge pattern to alleviate the effects of the numerical error in the applied field near the undulated surfaces; γ_v is calculated correspondingly from the particular total charge on the microtubule. Also, the ratio of the electrical conductivity is prescribed as $\sigma_p/\sigma_f = 0.001$.

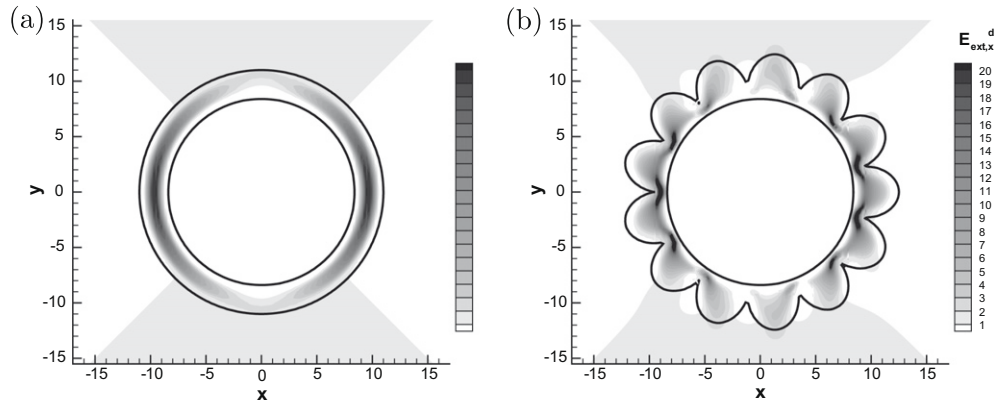

Fig. 15. *Applied electric field distorted by poorly-conducting hollow structures*: Comparison of the primary component of the dimensionless applied field $E^d_{ext,x} = E_{ext,x}/E_{\infty,x}$ between a cylinder (a) and a microtubule (b) of infinite spanwise length, with an external electric field of $\mathbf{E}_\infty = (4000, 0, 0)$ V/m and a ratio of $\sigma_p/\sigma_f = 0.001$.

Table 2
Electrophoretic velocity and anisotropy: different particles with same surface charge density. $V_{p\|}$ refers to particle velocity with parallel orientation with respect to the applied field, and $V_{p\perp}$ refers to perpendicular orientation.

	$V_{p\|}$ (m/s)	$V_{p\perp}$ (m/s)	*Anisotropy*
Exact, Solid cyl, infinite	10.38e−5	8.936e−5	0.861
Solid cyl, infinite	9.860e−5	8.391e−5	0.851
Hollow cyl, infinite	10.09e−5	8.109e−5	0.804
Microtubule, infinite	11.35e−5	8.964e−5	0.790
Microtubule, finite $L/a = 4$	8.132e−5	5.961e−5	0.731
Microtubule, finite $L/a = 8$	8.784e−5	6.790e−5	0.773
Microtubule, experiment, infinite	10.36e−5	8.6e−5	0.83

It is shown by Table 2 that the electrophoretic velocity of an infinite cylinder with transverse or parallel external field is resolved with errors of 5.0% and 6.1%, respectively. A hollow cylinder has a larger parallel mobility than a solid cylinder, which might come from the higher charge and hence larger electric force on the cylinder. In contrast, the transverse mobility of a hollow cylinder is smaller than the solid one, which may result from the oppositely charged fluid confined inside the cylinder. We also see that the mobilities of a microtubule are significantly larger than the ones for a hollow cylinder, which is again due to the higher net charge and hence larger electric driving force on the microtubule. Both the anisotropy and the individual mobilities of a microtubule are in close agreement with the experimental values reported in experiments of [27]

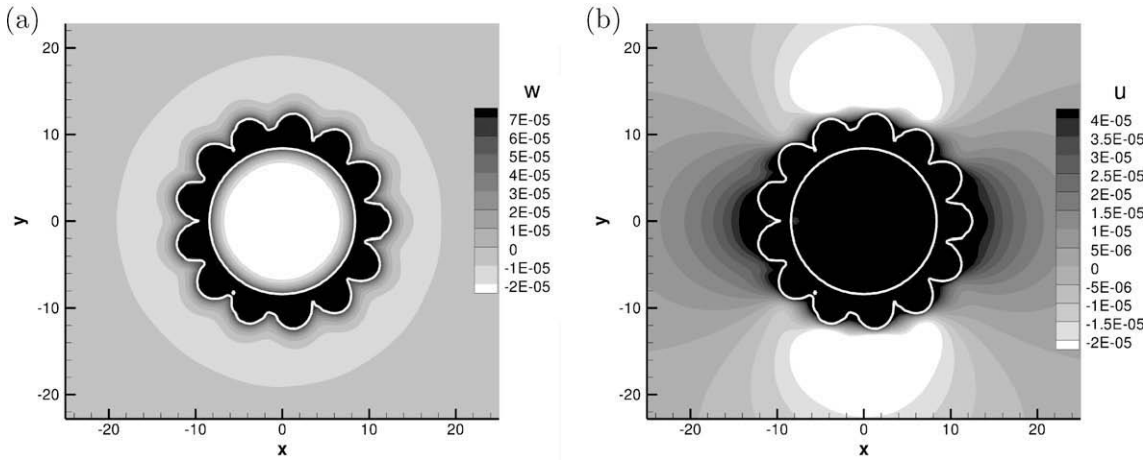

Fig. 16. *Electrophoresis of a microtubule of length $L/a = 4$ with either axial or perpendicular orientations*: Velocity contour in the cross-section $z = 0$, with an external electric field of $\mathbf{E}_\infty = (0, 0, 4000)$ V/m (a) and $\mathbf{E}_\infty = (4000, 0, 0)$ V/m (b).

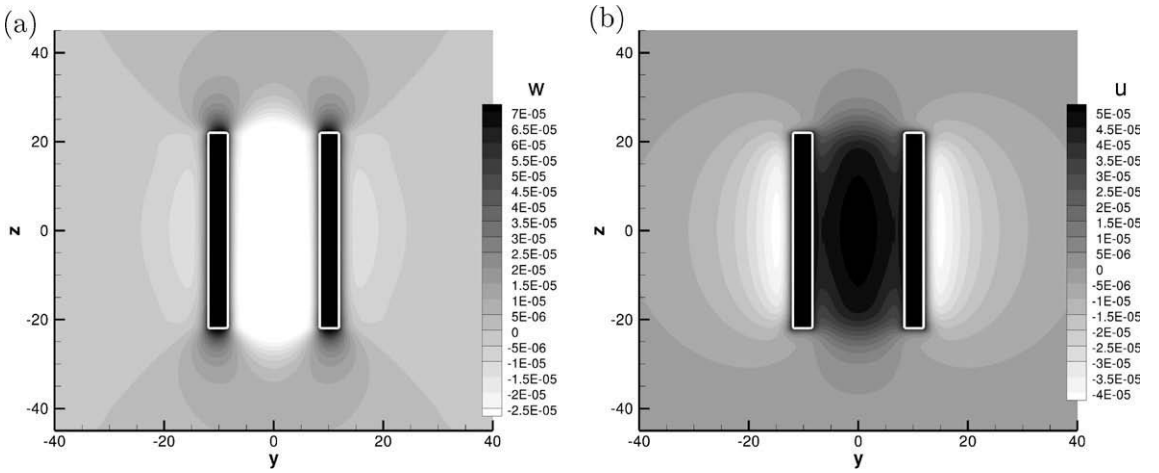

Fig. 17. *Electrophoresis of a microtubule of length $L/a = 4$ with either axial or perpendicular orientations*: Velocity contour in the axial plane $x = 0$, with an external electric field of **E**

and listed in the table here (5–10%), given all the uncertainties in both experimental and numerical set-ups. Furthermore, the table indicates that by reducing the length of the microtubule to a small value $L/a = 4$, the mobility and also the anisotropy drops significantly. Note that a different computational domain is used for finite microtubules, i.e. $[-88, 88] \times [-88, 88] \times [-165, 165]$ with 10,816 nonuniform rectilinear elements.

Figs. 16 and 17 show the electrophoretic motion of a microtubule with a spanwise length $L/a = 4$. It is indicated that compared to the infinite microtubules, such a limited spanwise dimension leads to a significant decrease in the mobilities. However, the finite structures disturb the surrounding fluid to a greater extent, e.g. a reverse flow is present outside the microtubule as shown in Fig. 16(a). Also, for the perpendicular orientation in Fig. 16(b), the non-uniformity of the inner fluid velocity is alleviated; this is due to the fact that the fluid inside is not fully confined anymore because of the open-ends. Fig. 17 further confirms these statements by showing a different angle of view, i.e. there exist large variations of the velocity near the free ends, and the outer fluid is influenced greatly by the finite dimension effects.

5. Summary and discussion

In this paper, we have developed a fast modeling method for electrokinetic flows where particles with arbitrary electrical conductivity are present. We modified the Poisson–Boltzmann (PB) and electric charge continuity equations based on a *smoothed profile* technique, to account for the entire domain including the particles. These equations were solved using the spectral element method in conjuction with the modified incompressible Navier–Stokes equations, to include the electrokinetic forces.

We verified the method by benchmark problems of electroosmotic flows in straight channels and by electrophoresis of charged cylinders. The modeling error of the coupled electrokinetic solver was quantified, and it showed a significant difference from the error behavior of the pure hydrodynamic solver. By excluding the error from the PB solution, we showed that the modeling error is non-monotonic; the optimum time step comes from a balance between the thickness of the Stokes diffusive layer and the one of the electrical diffuse layer, i.e. $\delta = 2.76\sqrt{vdt} \sim \lambda_d$. However, by solving the PB equation numerically we obtain a "fortuitous" cancellation of errors, for both planar and curved surfaces studied, which allows us to use large time steps and enhanced accuracy. We note, however, that in studying time-dependent flows a judicious balance between temporal error and SMP-modeling error should be pursued and this ultimately will determine the optimum time step for accuracy.

As the direct boundary conditions at particle/solution interfaces are removed, the proposed method is advantageous for simulating electrokinetic flows with moving complex-shaped particles which are charged. Simulation results for the electrophoresis of charged microtubules were presented for the first time and the simulated electrophoretic mobility and anisotropy agreed with the experimental results.

We note that further improvements can be made to the proposed modeling method. Since the accuracy limitation comes from the current continuity solver, a better approach can be used to solve for the "discontinuous" electric field, such as a discontinuous Galerkin formulation or a spectral filtering method or an ENO-type differentiation. Another limitation is due to the assumptions made in deriving the PB and current continuity equations. It is assumed that the charge distribution is in an equilibrium state, i.e. ionic advection is negligible. A more accurate model would be the Nernst–Planck equation [49,7] for ionic transport instead of the hypothesized Boltzmann distribution. A possible way to effectively solve the Poisson–Nernst–Planck equations would be to rewrite them to account for the entire domain by using a smooth approximation

of the diffusitivity D_i. However, since the transport processes of all the species are influenced by each other, the governing equations are coupled together, which poses a great challenge to numerical modeling.

Acknowledgment

This work was supported by NIH Grant Number R01 HL094270 and by NSF.

References

[1] Y. Nakayama, R. Yamamoto, Simulation method to resolve hydrodynamic interactions in colloidal dispersions, Physical Review E 71 (2005) 036707.
[2] R. Yamamoto, Y. Nakayama, K. Kim, A method to resolve hydrodynamic interactions in colloidal dispersions, Computer Physics Communications 169 (1–3) (2005) 301–304.
[3] K. Kim, Y. Nakayama, R. Yamamoto, Direct numerical simulations of electrophoresis of charged Colloids, Physics Review Letters 96 (2006) 208302.
[4] X. Luo, M.R. Maxey, G.E. Karniadakis, Smoothed profile method for particulate flows: error analysis and simulations, Journal of Computational Physics 228 (2009) 1750–1769.
[5] K.A. Sharp, B. Honig, Electrostatic interactions in macromolecules-theory and applications, Annual Review of Biophysics and Biophysical Chemistry 19 (1990) 301–332.
[6] D.J. DePaolo, F.M. Orr, Basic research needs for geosciences: Facilitating 21st century energy systems, Office of basic energy sciences, US Department of Energy, 2007.
[7] R.F. Probstein, Physicochemical Hydrodynamics, Wiley, 1994.
[8] G. Karniadakis, A. Beskok, N. Aluru, Microflows and Nanoflows: Fundamentals and Simulation, Springer, 2005.
[9] P. Wang, Z.L. Chen, H.C. Chang, A new electroosmotic pump based on silica monoliths, Sensors and Actuators B 113 (2006) 500–509.
[10] J. Molho, A.E. Herr, M. Desphande, J.R. Gilbert, M.G. Garguilo, P.H. Paul, P.M. John, T.M. Woudenberg, C. Connel, Fluid transport mechanisms in micro fluidic devices, in: ASME International Mechanical Engineering Congress and Exposition, 1998, pp. 69–75.
[11] E.B. Cummings, S.K. Griffiths, R.H. Nilson, Irrotationality of uniform electroosmosis, in: Proc. SPIE Microfluidic Devices and Systems II, 1999, pp. 180–189.
[12] M.J. Kim, K.D. Kihm, A. Beskok, A comparative study of μ-PIV measurements and numerical simulations of electroosmotic flows in various microchannel configurations, Experiments in Fluids 33 (2002) 170–180.
[13] A. Singh, E.B. Cummings, D.J. Throckmorton, Flourescent liposome flow markers for microscale particle-image velocimetry, Analytical Chemistry 73 (5) (2001) 1057–1061.
[14] A.E. Herr, J.I. Molho, J.G. Santiago, M.G. Mungal, T.W. Kenny, M.G. Garguilo, Electroosmotic capillary flow with non uniform zeta-potential, Analytical Chemistry 72 (2000) 1053–1057.
[15] C. Yang, D. Li, Analysis of electrokinetic effects on the liquid flow in rectangular microchannels, Journal of Colloids and Surfaces 143 (1998) 339–353.
[16] N. Patankar, H.H. Hu, Numerical simulation of electroosmotic flow, Analytical Chemistry 70 (9) (1998) 1870–1881.
[17] P. Dutta, A. Beskok, T. Warburton, Electroosmotic flow control in complex microgeometries, Journal of Microelectromechanical Systems 11 (1) (2002) 36–44.
[18] P. Dutta, A. Beskok, T. Warburton, Numerical simulation of mixed electroosmotic/pressure-driven microflows, Numerical Heat Transfer Part – A: Applications 41 (2) (2002) 131–148.
[19] J. Hahm, A. Balasubramanian, A. Beskok, Flow and species transport control in grooved microchannels using local electrokinetic forces, Physics of Fluids 19 (1) (2007) 013601.
[20] M.J. Mitchell, R. Qiao, N.R. Aluru, Meshless analysis of steady state electroosmotic transport, Journal of Microelectromechanical Systems 9 (4) (2000) 435–449.
[21] R. Qiao, N.R. Aluru, A compact model for electroosmotic flows in microfluidic devices, Journal of Micromechanics and Microengineering 12 (5) (2002) 625–635.
[22] J.K. Wang, M. Wang, Z.X. Li, Lattice Poisson–Boltzmann simulations of electroosmotic flows in microchannels, Journal of Colloid and Interface Science 296 (2006) 729–736.
[23] G.H. Tang, Z. Li, J.K. Wang, Y.L. He, W.Q. Tao, Electroosmotic flow and mixing in microchannels with the lattice Boltzmann method, Journal of Applied Physics 100 (9) (2006) 094908.
[24] J.D. Watson, T.A. Baker, S.P. Bell, A. Gann, M. Levine, R. Losick, Molecular Biology of the Gene, Cold Spring Harbor Lab. Press, San Francisco, CA: Benjamin Cummings/New York, 2004.
[25] M.G.L. van den Heuvel, M.P. de Graaff, C. Dekker, Molecular sorting by electrical steering of microtubules in Kinesin-coated channels, Science 312 (5775) (2006) 910–914.
[26] A.V. Delgado1, F. Gonzolez-Caballero1, R.J. Hunter, L.K. Koopal, J. Lyklema, Measurement and interpretation of electrokinetic phenomena, Pure and Applied Chemistry 77 (10) (2005) 1753–1805.
[27] M.G.L. van den Heuvel, M.P. de Graaff, S.G. Lemay, C. Dekker, Electrophoresis of individual microtubules in microchannels, Proceedings of the National Academy of Sciences 104 (19) (2007) 7770–7775.
[28] G.L. Li, Q. Wen, J.X. Tang, Single filament electrophoresis of f-actin and filamentous virus fd, Journal of Chemical Physics 122 (2005) 104708.
[29] D.C. Henry, Electrokinetic flow in ultrafine capillary slits, Proceedings of the Royal Society London Series 133 (821) (1931) 106–129.
[30] W.B. Russel, D.A. Saville, W.R. Schowalter, Colloidal Dispersions, Cambridge University Press, 1989.
[31] H. Ohshima, A simple expression for Henry's function for the retardation effect in electrophoresis of spherical colloidal particles, Journal of Colloid and Interface Science 168 (1994) 269–271.
[32] H. Ohshima, Henry's function for electrophoresis of a cylindrical colloidal particle, Journal of Colloid and Interface Science 180 (1996) 299–301.
[33] R.W. O'Brien, L.R. White, Electrophoretic mobility of a spherical colloidal particle, Journal of the Chemical Society. Faraday Transactions II 74 (1978) 1607–1626.
[34] N. Baker, M. Holst, F. Wang, Adaptive multilevel finite element solution of the Poisson–Boltzmann equation II. refinement at solvent-accessible surfaces in biomolecular systems, Journal of Computational Chemistry 21 (2000) 1343–1352.
[35] L. Chen, M.J. Holst, J.C. Xu, The finite element approximation of the nonlinear Poisson–Boltzmann equation, SIAM Journal on Numerical Analysis 45 (2007) 2298–2320.
[36] K. Kim, Y. Nakayama, R. Yamamoto, Direct numerical simulations of electrophoresis of charged colloids, Physics Review Letters 96 (2006) 208302.
[37] R. Yamamoto, K. Kim, Y. Nakayama, Strict simulations of non-equilibrium dynamics of colloids, Colloids and Surfaces A: Physicochemical and Engineering Aspects 311 (1–3) (2007) 42–47.
[38] Y. Nakayama, K. Kim, R. Yamamoto, Simulating (electro)hydrodynamic effects in colloidal dispersions: Smoothed profile method, European Physical Journal E 26 (2008) 361–368.
[39] G. Gouy, Sur la constitution de la electrique a la surface d'un electrolyte, Journal of Physics Radium 9 (1910) 457.
[40] D. Chapman, A contribution to the theory of electroencapillarity, Philosophical Magazine 25 (6) (1910) 475.
[41] R.P. Feynman, R.B. Leighton, M. Sands, The Feynman Lectures on Physics, Addison-Wesley, Massachusetts, 1977.
[42] B. Honig, A. Nicholls, Classical electrostatics in biology and chemistry, Science 268 (1995) 1144–1149.

[43] D. Funaro, D. Gottlieb, A new method of imposing boundary conditions in pseudospectral approximations of hyperbolic equations, Mathematics of Computation 51 (184) (1988) 599–613.
[44] J.S. Hesthaven, D. Gottlieb, A stable penalty method for the compressible Navier–Stokes equations: I. open boundary conditions, SIAM Journal on Computing 17 (3) (1996) 579.
[45] G.E. Karniadakis, S.J. Sherwin, Spectral/hp Element Methods for CFD, Oxford University Press, New York, 1999.
[46] J. Israelachvili, Intermolecular and Surface Forces, Academic, London, 1992.
[47] H. Ohshima, Surface charge density/surface potential relationship for a cylindrical particle in an electrolyte solution, Journal of Colloid and Interface Science 200 (2) (1998) 291–297.
[48] I.A. Schaap, C. Carrasco, P.J. de Pablo, F.C. MacKintosh, C.F. Schmidt, Elastic response, buckling, and instability of microtubules under radial indentation, Biophysical Journal 91 (4) (2006) 1521–1531.
[49] P.C. Lichtner, Principles and practive of reactive transport modeling, Material Research Society of Symposium on Proceedings 353 (1995) 117–130.